Research Article

Analysis for Shear Behavior of SRC Deep Beams Based on Tests, Digital Image Correlation Technique, and Finite Elemental Simulation

Buqing Chen [ID],[1] Jun Wu [ID],[1,2] Changjun Liu,[1] Yanhua Liu,[1] Wenmei Zhou,[1] and Yunfeng Xiao[3]

[1]*School of Urban Construction, Yangtze University, Jingzhou 434023, China*
[2]*Beijing Building Materials Acacemy of Sciences Research, Beijing 100043, China*
[3]*School of Civil and Hydraulic Engineering, Huazhong University of Science and Technology, Wuhan 430074, China*

Correspondence should be addressed to Jun Wu; wujun737@yangtzeu.edu.cn

Seven steel-reinforced concrete (SRC) deep beams were tested to investigate the shear performance, including peak loads, failure modes, mid-span deflections, and cracking patterns. The parameters include the shear span-to-depth ratio and the dimensions of the steel skeleton. The digital image correlation (DIC) technique was utilized for real-time recording of the in-plane strain and deformation. The experiment results show that the failure modes of specimens could be concluded as two forms: diagonal compression failure and shear failure. The DIC technique was proved to be efficient for tracking the development of crack patterns and recording the failure modes. The corresponding numerical analyses based on experiments were carried out and demonstrated to be a reliable method to simulate the shear response. Furthermore, the most significant parameters and their interactions were identified by finite element models parameter analysis. The steel skeleton height and shear span-to-depth ratio were the main parameters affecting shear capacity. A design formula based on the strength superposition method was presented. The calculated results were basically in agreement with the test results, where the mean and coefficient of variation were 1.04 and 0.09, respectively.

1. Introduction

The steel-reinforced concrete (SRC) deep beam is a composite member formed by built-in steel sections. Due to good seismic performance, high shear capacity, and ductility, SRC deep beams have been widely used in housing construction, bridges, and underground engineering [1–4], especially the gigantic transition beams of complicated high-rise building structures [5–8].

Few codes give a clear definition of the SRC deep beams. Generally, the definition of the reinforced concrete (RC) deep beams is used to define the SRC deep beams. ACI 318-19 defines deep beams as beams whose shear span-to-depth ratio does not exceed 2 [9]. Previous studies [10, 11] have shown that the mechanical properties of SRC deep beams are quite different from those of slender beams. Due to the small

span-depth ratio, its bearing capacity is controlled by shear stress instead of bending stress. The section of SRC deep beam under concentrated load causes bending normal stress, shear stress, and compressive stress simultaneously, resulting in a complex and nonlinear strain distribution.

A suitable calculation model is a basis for understanding the shear transfer mechanism and predicting the bearing capacity. According to the recommendations of the design code including ACI 318-19 [9] and EC-2 [12], the Strut-and-Tie Model (STM) is applied to calculate the shear capacity of deep beams. To optimize and enhance the accuracy of the model, many scholars have proposed various modified STMs. Hwang SJ and Lee [13] proposed a softened STM to predict the destructive strength of discontinuous areas in diagonal compression of concrete. Lu [10] calculated the shear capacity based on softening STM and considering the

combined action of the internal steel skeleton and concrete. Chen et al. [11] considered the depth of the steel skeleton as a major influence parameter and derived an SST-SRC model to predict the shear capacity of SRC deep beams. However, the STM model is based on the theory of lower plastic limit values, with various forms. It is very important whether the established model can truly reflect the real force. At the same time, establishing an effective STM is a hard problem. Additionally, for SRC structural members, the concept of strength superposition is recommended by many design codes including the AIJ Standard [14] and the JGJ 138-2016 [15]. Weng and Wang [16] studied the influence of shear studs and stirrups on the shear behavior of SRC deep beams. The shear capacity of SRC members is divided into the RC part and the steel skeleton part. Based on the strength superposition method, the shear capacity is affected by many parameters of the component, such as the concrete tensile strength, web and flange of steel skeleton, shear span-to-depth ratio, longitudinal reinforcement ratio, and stirrups. However, the above research including the modified Strut-and-Tie Models predicted the shear capacity by describing the load transfer path, whereas many influence parameters were not discussed. Furthermore, the strength superposition method was mostly used to analyze slender beams; only a few influence parameters of deep beams were analyzed. Existing studies cannot fully consider the changing trend of shear capacity. Therefore, studying the factors of the effect of the shear capacity of SRC deep beams and establishing an accurate method for predicting shear capacity were urgently important issues.

The traditional measuring tools were used in many structural tests, such as strain gauges, displacement transducer, and extensometer. But the disadvantage of these tools is that they can only measure the strain in a certain area. The strain gauge will fail once the concrete cracks and cannot record the full-field strain of the surface of the beams. Due to the complex stress state of SRC deep beams, it is difficult for traditional measuring tools to capture the variation law of concrete surface strain. Thus, in order to continuously and accurately observe the shear response and cracking pattern of SRC deep beams, the digital image correlation (DIC) technology was applied to this experiment. This technology is a noncontact modern optical measurement technology, which has the merits of a simple measuring device, strong environmental adaptability, and a wide measurement range. Thus, it has been widely used in civil engineering, mechanical, materials science, and other scientific or engineering fields [17]. Its basic principle is to get the displacement by tracking the position of the same pixel in the two speckle images before and after the surface deformation, thereby obtaining the whole field displacement and strain of the surface. This technology overcomes the shortcomings of traditional strain gauge measurement and naked eye identification of cracks, which can continuously observe the development of crack and surface strain [18]. Therefore, the DIC technique was used to study the shear cracking response, crack pattern, initial crack load, and location and track the crack development of SRC deep beams.

In this paper, seven SRC deep beams were tested to study the shear performance using the DIC technique. The influence of the shear span-to-depth ratio and the size of the steel skeleton on the shear response were investigated. Furthermore, the finite element models were established and verified with good agreement. Besides, the effect of reinforcement ratio, stirrup spacing, and concrete strength on shear capacity was further studied by a series of parameter analyses. According to the strength superposition theory, the calculation formula of shear bearing capacity was proposed. The results can provide a reference for predicting the shear performance of SRC deep beams.

2. Test Program

2.1. Test Specimen Design and Material Properties. All specimen sizes were designed according to the facilities of the laboratory. Half-scale specimens were selected for this paper because deep beams of this size were large enough to capture essential response phenomena experienced by full-scale deep beams, while they were small enough to keep the overall project costs within budget. The reinforcements were arranged based on the permissible range of ACI 318-19. The dimensions of the steel skeleton and reinforcement drawings are shown in Figure 1. All SRC deep beams have the same cross-sectional dimension of $180 \, mm \times 320 \, mm$. Two $18 \, mm$ diameter longitudinal bars are arranged at the top of the beam section while four are arranged at the bottom. The stirrups consisted of $\phi 6@100 \, mm$ steel bars. The H-shaped steel skeleton was embedded inside the beams. Table 1 shows the main parameters of specimens. The main research parameters are the height of the steel skeleton, the shear span-to-depth ratio λ, and the width of the steel skeleton flange. The specimens are designed in three lengths, including $860 \, mm$, $1020 \, mm$, and $1200 \, mm$, respectively. A total of five different dimensions of steel skeleton were studied. RDB-1, RDB-2, and RDB-3 had the same properties, except λ varied from 1.1 to 1.7.

All the specimens were cast-in-place. The concrete used in the study was provided by a local supplier, with a maximum aggregate size of 20 mm. The target compressive strength is C40. On the day of testing, three sizes of 150 mm(length) × 150 mm(width) × 300 mm(height) prisms and three cubes with 150 mm edges were reserved for each test beam. Three prisms were used to measure the compressive and three cubes are used to measure splitting tensile strengths. According to the Chinese standard GB/T 50081 [19], the average concrete compressive strength f_c was 25.2 MPa and the average tensile strength f_t was 2.14 MPa; besides, the elastic modulus was 3.31×10^4 MPa. The longitudinal reinforcements and the stirrups are in grade HRB335 and HPB300 hot rolled reinforced bars, respectively. The steel skeleton is hot rolled H-shaped steel with grade Q235. Table 2 shows the properties of reinforcements and steel.

2.2. Test Setup. Figure 2 shows the schematic diagram of the test. A three-point bending monotonic static load test method is applied to the specimen. The YHD-50 displacement sensor was fixed at the bottom of the beam to record the central displacement. Two dial gauges were installed near
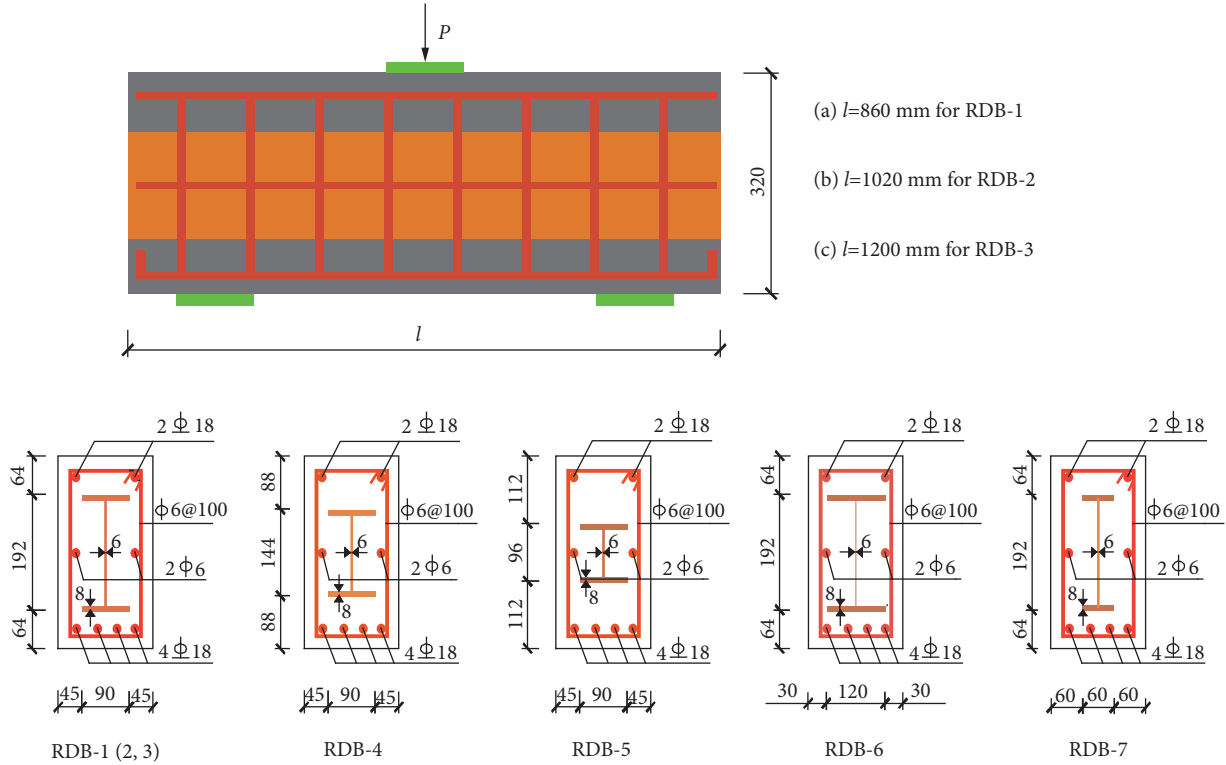
FIGURE 1: Dimensions and reinforcements of specimens.

TABLE 1: Main parameters of SRC beams.

Specimens	Length (mm)	λ	Width ratio	Height ratio	Cross section of H-shaped steel (mm)
RDB-1	860	1.1	0.5	0.6	$192 \times 90 \times 6 \times 8$
RDB-2	1020	1.4	0.5	0.6	$192 \times 90 \times 6 \times 8$
RDB-3	1200	1.7	0.5	0.6	$192 \times 90 \times 6 \times 8$
RDB-4	860	1.1	0.5	0.45	$144 \times 90 \times 6 \times 8$
RDB-5	860	1.1	0.5	0.3	$96 \times 90 \times 6 \times 8$
RDB-6	860	1.1	0.67	0.6	$192 \times 120 \times 6 \times 8$
RDB-7	860	1.1	0.33	0.6	$192 \times 60 \times 6 \times 8$

TABLE 2: Measured material characteristics of steels.

Steel grade	Diameter/thickness (mm)	Yield strength f_u (MPa)	Ultimate strength f_u (MPa)	Young's modulus E_s (MPa)
HPB300	6	313	534	2.1×10^5
HRB335	18	440	515	2.1×10^5
Q235	6	272	406	2.0×10^5
	8	315	430	2.0×10^5

the supports to observe the angle of rotation. The strain gauges were attached to the longitudinal reinforcement, stirrups, and steel skeleton to measure strains, as shown in Figures 2(a) and 2(b).

A 2D digital image correlation (DIC) method was applied to monitor surface full-field strain of concrete, displacement, and the crack pattern of specimens. The system consists of a single camera and a light source as shown in Figures 2(c) and 2(d). The surface of the observation area is kept parallel to the image plane of the camera throughout the measurement process. The system was able to measure an

approximately 430–600 mm wide area from the center to the end of the beams, corresponding to the moment-shear area. The speckle spots of the specimen are drawn manually, and the white light source was used to ensure that a clear picture of the experiment was captured. The experimental device is tested in conjunction with DIC digital camera, and the images were captured every 10 kN. The analysis is completed using a subset size of 41 pixels, a step size of 5 pixels.

The electrohydraulic servo actuator is employed to apply load by means of the displacement controlled method. When the applied load on the specimens dropped below 85%
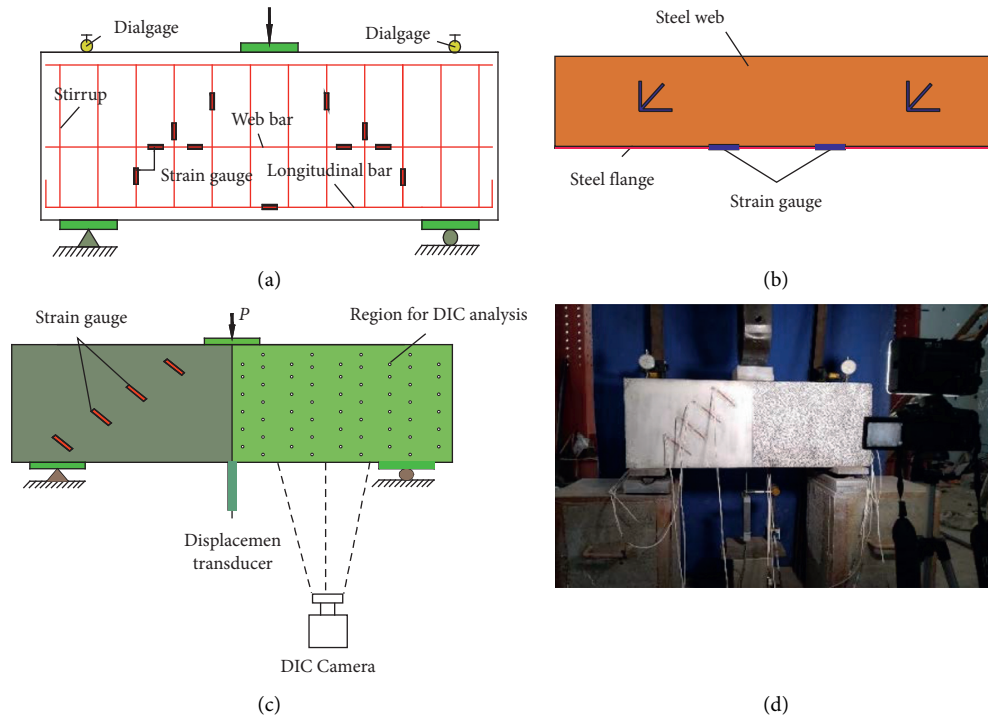
FIGURE 2: The schematic diagram of the test setup. (a) Typical instrumentation of the beam. (b) Strain position of steel shape. (c) Schematic of the DIC test loading system. (d) Test method system.

of the peak load or obvious failure occurred, the tests were stopped. All data of strain gauges, load, and displacement transducer were registered corresponding to DIC images using a data acquisition system. In the process of testing, the initial shear and flexural cracking load and crack patterns at each stage were recorded.

2.3. Test Results. Figures 3 and 9 show the failure modes and the load-deflection curves of specimens. The DIC technique was used to record the crack patterns and study the cracking process during the test. Under concentrated load, the failure modes of seven test specimens were concluded as two forms: (a) diagonal compression failure and (b) shear failure. The test results including cracking loads, peak loads, mid-span deflections, and failure modes are listed in Table 3.

The diagonal compression failure occurred in the specimens RDB-1 and RDB-4~RDB-7. These beams mainly failed by the crushing of concrete from the loading point to the support. The λ ($\lambda = 1.1$) of these specimens are smaller than the others. Failure usually occurs along one of the main diagonal cracks. For a clear description of the diagonal compression, specimen RDB-1 is taken as an example; its failure mode and the measured load-deflection curve are shown in Figures 3(a) and 9(a). Before cracking, the load-deflections response of the beam was completely dominated by the bending stiffness. As the load increased, the cracks appeared gradually, which led to the decrease of stiffness and the large deformation. All test specimens exhibited vertical cracks prior to the diagonal cracking. The vertical concrete cracks in the beam RDB-1 commenced under the load of 90 kN at the bottom of the mid-span surface. But unlike

RDB-2 and RDB-3, the vertical cracks did not develop further. The diagonal cracks occurred soon after the vertical cracks appeared. Because λ ($\lambda = 1.1$) of such beams was relatively small, the bending moment effect at the mid-span was not obvious. The concrete diagonal compressive strut from the loading point to the support was subjected to a larger load.

The primary diagonal crack initiated approximately at the middle of the beam section at a load of 110 kN. Then, as the load increased, it extended to the support and the loading point. The same crack propagated to the diagonal compression zone up to peak load ($F_p = 788$ kN). When the peak load was reached, the specimen failed suddenly without warning and exhibited a brittle failure mode. At this time, a serious diagonal crack emerged on the concrete failure surface, and the bearing capacity of the specimen decreased rapidly. At ultimate load ($F_u = 680$ kN), the displacement in the beam mid-span of beam reached 8.6 mm and the width of the diagonal cracks further increased. The strains of stirrups close to diagonal cracks reached their yielding value and were bigger than those stirrups which were far from the cracks. Similarly, the strains of steel skeleton web embedded in the beam had also reached their yielding value. But, no longitudinal reinforcement yielded during the test procedure. The cracks at the bottom of the specimen were only slightly developed. Probably, the bending moment in the beam mid-span was small, resulting in the fact that the longitudinal reinforcement at the bottom was subject to tensile force slightly.

The specimens RDB-2 and RDB-3 with large λ ($\lambda = 1.4$ and 1.7) had experienced shear failure. Figures 3(c) and 3(d)
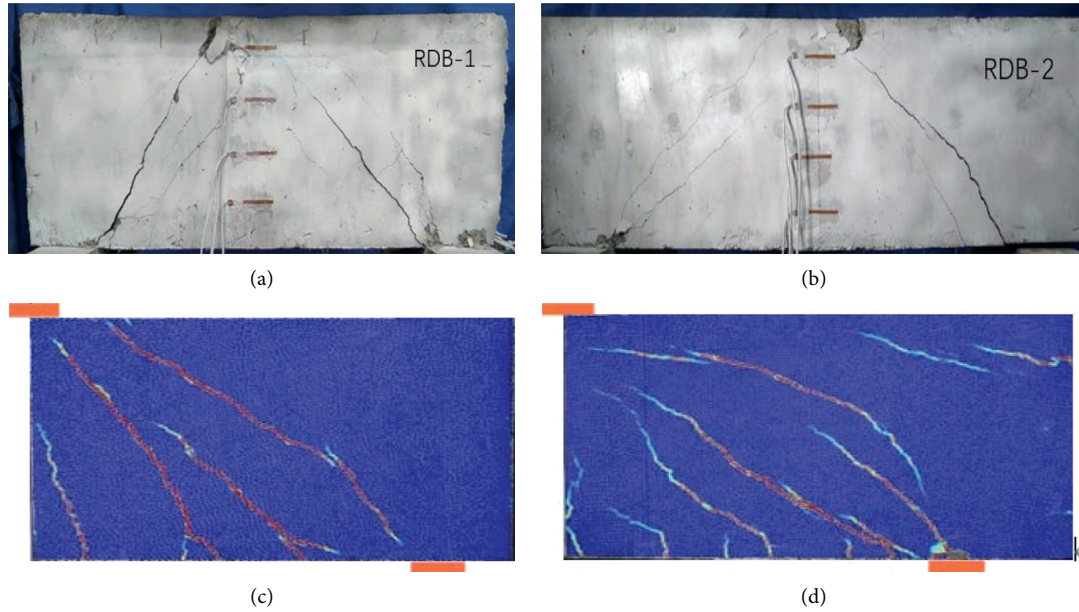
FIGURE 3: Failure modes and crack pattern. (a) Diagonal compression failure. (b) Shear failure. (c) Crack patterns of RDB-1 recorded by DIC. (d) Crack patterns of RDB-2 recorded by DIC.

TABLE 3: The test results of seven SRC deep beams.

Specimens	Shear cracking load (kN)	Peak load (kN)	Deflections (mm)	Failure modes
RDB-1	110	788	8.6	Diagonal compression
RDB-2	100	682	9.1	Shear
RDB-3	130	548	9.5	Shear
RDB-4	120	734	7.6	Diagonal compression
RDB-5	130	645	8.9	Diagonal compression
RDB-6	160	816	9.8	Diagonal compression
RDB-7	100	698	8.1	Diagonal compression

show the failure mode and crack pattern of RDB-2. It can be clearly seen that there are many cracks distributed on the shear span area of the beams. These beams mainly failed by the crushing of concrete at the shear span area. The cracks that ultimately lead to beam failure are diagonal shearing cracks rather than bending cracks. Hence, the failure mode of beams RDB-2 and RDB-3 is defined as shear failure.

The vertical cracks in the mid-span surface of beam RDB-2 were initiated under 60 kN load and they propagated up to load 100 kN until diagonal cracks occurred. As expected, these vertical cracks gradually extended up to about two-thirds of the beam section height by increasing load. A large number of cracks occurred densely in the shear span area. From Figure 3, a smaller spacing between the diagonal cracks can be seen for beams with larger λ. As the load increased further and enhanced the bending moment, the mid-span displacement expanded. At the ultimate load ($F_u = 590$ kN), the displacement reached 9.1 mm. Similarly, in beam RDB-3, at ultimate load ($F_u = 460$ kN), the displacement reached 9.5 mm. Both RDB-2 and RDB-3 failed in larger displacement and the better ductile mode is shown. The experimental data showed that the strains of longitudinal reinforcement at the bottom reached a yielding value.

As with other beams, strain measurements indicated that the stirrups and steel skeleton webs at the diagonal cracks of the beams all reached the yielding value. From Table 3, it can be shown that the shear capacity decreases with the increase of λ. When λ varied from 1.1 to 1.7, the shear capacity decreased by 31%. In addition, the steel skeleton flange and web also have a positive influence on the shear capacity. When the web height ratio increased from 0.3 to 0.6, the shear capacity increased by 22%. When the flange width ratio increased from 0.33 to 0.67, the shear capacity increased by 17%.

3. Finite Element Analysis

Three-dimensional finite element models (FEMs) have been developed to simulate the nonlinear shear response of the SRC deep beams based on the ABAQUS software. The simulation results were compared with those of experimental results. The relevant parameters affecting the shear response were further studied by FEM. Then, the relationship between the research parameters and the shear capacity of SRC deep beams was established by the finite element analysis.

3.1. General Details. Figure 4 shows the typical FEM of the SRC deep beam. Except for the reinforcement bars, all parts are simulated using solid elements (C3D8R). This element only contains an integral point in the center of the element, and the shear self-locking is difficult to occur under the bending load. Moreover, the analytical accuracy of the C3D8R element could not be greatly affected when the mesh is distorted, and it solves the displacement problem more accurately. The reinforcement bars are simulated using two-node truss elements (T3D2). All bars are merged into a whole. Since no bonding failure of the internal reinforcement bars, steel skeleton, and surrounding concrete was observed in the test, it is assumed that they are perfectly bonded. Therefore, the longitudinal bars, stirrups, and steel skeleton are "embedded" in the concrete. Reinforcement bars and steel skeleton were meshed with elements of 25 mm in length. The size of the concrete element is 25 mm at the analysis position and 50 mm at the edge of beams. The rigid steel was modeled using solid elements C3D8R to avoid stress concentration at concrete loading points and supports. "Tie" command was applied for the contact between supports and concrete. The material properties of rigid steel are elastic modulus of 2.1×10^{12} Pa and the Poisson ratio of 0.3. Furthermore, in the ABAQUS standard procedure, the parameter NLGEOM was activated to consider the large displacement.

3.2. Material Modeling of Steel. The material behaviors of steel reinforcement and steel skeleton were assumed as a nonlinear elastic-plastic. The nonlinear stress (σ)-strain (ε) model proposed by Chinese code GB 50010-2010 [20] for steel material is shown in Figure 5. The classical metal plasticity model was used in plasticity analysis. In ABAQUS, the classic metal plasticity models use the standard Mises yield surface and associated plastic flow to achieve the isotropic yield, while also providing the definition of perfect plasticity and isotropic hardening. Because the experimentally measured data is nominal stress-strain data, equations (2) and (3) need to be converted into true stress and logarithmic strain data before inputting into ABAQUS. where σ_s is the stress of steel skeleton and reinforcing bars; E_s is Young's modulus; ε_s is the strain of steel skeleton and reinforcing bars; k is the slope of the hardening section of steel; f_y is the yield strength; ε_y is the strain at the yield strength; f_{st} is the ultimate strength of steel; and ε_u is the strain at the ultimate strength.

$$\sigma_s = \begin{cases} E_s \varepsilon_s, & \varepsilon_s \leq \varepsilon_y, \\ f_y + k(\varepsilon_s - \varepsilon_y), & \varepsilon_y < \varepsilon_s \leq \varepsilon_u, \end{cases} \tag{1}$$

$$\sigma_{ture} = \sigma_{nom}(1 + \varepsilon_{nom}), \tag{2}$$

$$\varepsilon_{In}^{pl} = \ln(1 + \varepsilon_{nom}) - \frac{\sigma_{ture}}{E}, \tag{3}$$

where σ_{ture} is the true stress; σ_{nom} is the nominal stress; ε_{In}^{pl} is the logarithmic strain; and ε_{nom} is the nominal strain.

3.3. Material Modeling of Concrete. The nonlinear response of concrete in the test beam was simulated by using the CDP model. The damage and stiffness degradation of concrete has been considered by the CDP model that was proposed according to the research of Lubliner et al. [21] and the revision of Lee and Fenves [22]. In ABAQUS, not merely concrete materials but also some quasi-brittle materials can be simulated with the CDP model in all different types of structures including solid elements.

The five main parameters need to be determined in the CDP model. The default flow potential eccentricity $\epsilon = 1$. The dilation angle (ψ) is an important parameter to defined nonassociated potential plastic flow. Its value usually ranges from $0°$ to $56°$ [23]. In this study, based on conducting a sensitivity analysis, the value $35°$ was used. The default value parameter f_{b0}/f_{c0} is 1.16. The parameter K_c must meet the conditions $0.5 < K_c \leq 1.0$. This paper takes the default value 2/3. Usually, the viscoelastic regularization of the small value of the viscosity coefficient μ helps to increase the convergence rate of the model during the softening stage without affecting the results. Thus, a value of 0.005 was taken.

The concrete stress-strain response in tension and compression was simulated using the relationship provided in the code GB 50010-2010 [20]. Figure 6 presents the stress-strain curve of concrete. The concrete stress-strain response in compression can be used by the following relation: where E_c is elastic modulus; α_c is the parameter value of the descending section; εcr is the peak compressive strain of concrete; f_{cr} is the uniaxial compression strength of concrete; and d_c is the damage parameter of concrete.

$$\begin{aligned} \sigma &= (1 - d_c)E_c\varepsilon, \\ d_c &= \begin{cases} 1 - \dfrac{\rho_c n}{n - 1 + x^n}, & x \leq 1, \\ 1 - \dfrac{\rho_c}{\alpha_c(x-1)^2 + x}, & x > 1, \end{cases} \\ \rho_c &= \frac{f_{cr}}{E_c\varepsilon_{cr}}, \\ n &= \frac{E_c\varepsilon_{cr}}{E_c\varepsilon_{cr} - f_{cr}}, \\ x &= \frac{\varepsilon}{\varepsilon_{cr}}. \end{aligned} \tag{4}$$

The concrete stress-strain response in tension can be used by the following relation:

$$\begin{aligned} \sigma &= (1 - d_t)E_c\varepsilon, \\ d_t &= \begin{cases} 1 - \rho_t\left[1.2 - 0.2x^5\right], & x \leq 1, \\ 1 - \dfrac{\rho_t}{\alpha_t(x-1)^{1.7} + x}, & x > 1, \end{cases} \\ x &= \frac{\varepsilon}{\varepsilon_{tr}}, \\ \rho_t &= \frac{f_{tr}}{E_c\varepsilon_{tr}}, \end{aligned} \tag{5}$$

where α_t is the parameter value of the descending section; ε_{tr} is the peak tension strain of concrete; f_{tr} is the uniaxial tension strength of concrete; and d_t is the damage parameter of concrete.
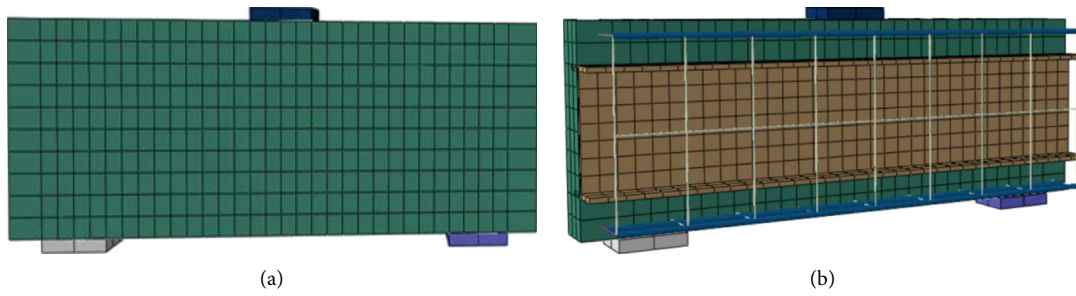
(a)

(b)

FIGURE 4: Typical FEM meshing of the SRC deep beam. (a) FEM meshing of concrete. (b) FEM meshing of reinforcement bars and steel skeleton.
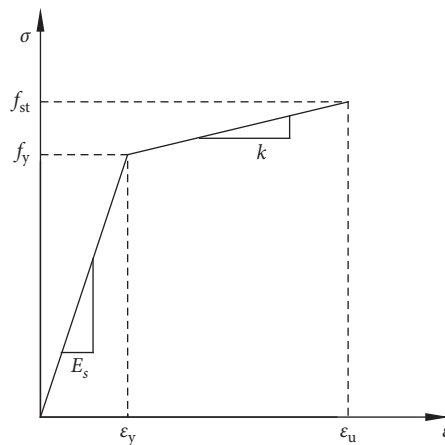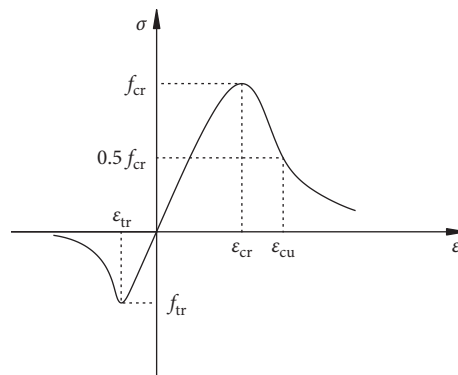

FIGURE 5: The stress-strain curve of steel.

FIGURE 6: The stress-strain curve of concrete.

3.4. FEM Validation. In ABAQUS, the CDP model cannot clearly output the cracks at the material integration point. However, the concept of effective crack direction can be introduced to acquire the graphical visualization of crack patterns in concrete structures. The vector direction perpendicular to the crack plane is assumed to be parallel to the direction of the maximum principal plastic strain. At the same time, the concept of equivalent plastic strain (PEEQ) is introduced in ABAQUS. When the PEEQ is greater than 0, the material has yielded. It is the cumulative result of plastic deformation during the whole deformation process.

According to the above methods for determining the crack patterns, the maximum principal plastic strain and PEEQ contour plots are reported in this study. The comparison between crack patterns from FEM and those recorded by DIC is shown in Figure 7. Figure 8 presents the comparison between failure mode from the test and the PEEQ of FEM. It can be clearly noticed that experimental and finite element models have similar failure modes. The shear diagonal cracks extended between the loading point and the support. The pattern and development process of cracks obtained by numerical simulation are consistent with the experimental specimen. The FEM can precisely capture and simulate the failure modes of SRC deep beams.

Figure 9 shows the load-deflection curves of the test and FEM in the mid-span of all specimens. At each stage of
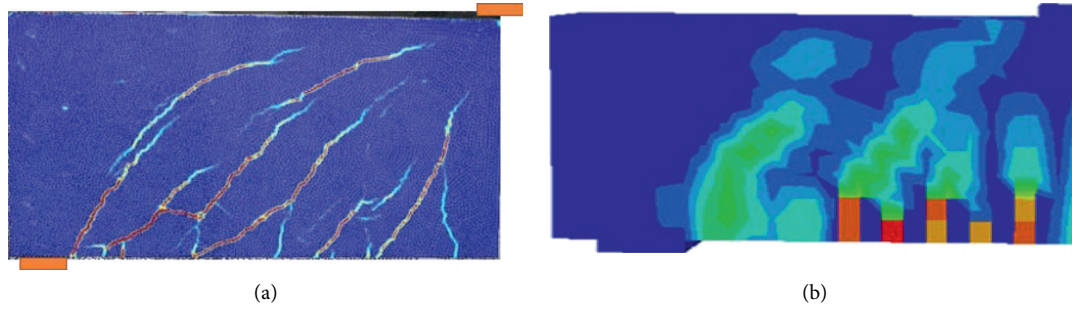
(a)

(b)

Figure 7: Comparison of crack pattern from FEM and recorded by DIC of RDB-3.
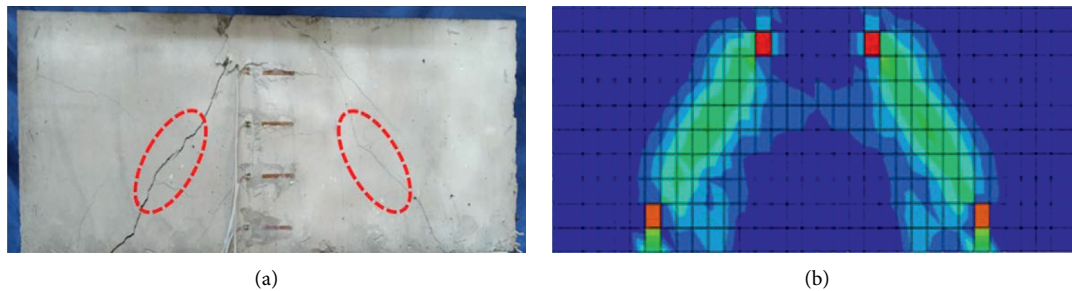

(a)

(b)

Figure 8: Comparison of failure modes between experimental and FEM of RDB-5.

loading, the results of predicted FEM load and deflection agree well with the test data. All curves are almost linear at the beginning of the load, before the crack forms. Subsequently, the curves are converted nonlinearly due to the stiffness degradation caused by the cracking of the specimen. The shear diagonal cracks developed with increased loading until the specimen was destroyed. After reaching the peak load, the bearing capacity of the specimen begins to decrease. By analyzing the results of FEM and the experimental, the accuracy of the FEM in simulating the nonlinear response of the experimental beam was further verified.

Furthermore, the FEM simulated the shear capacity with accuracy. The average simulated-to-test ratio of shear capacity was 1.05, and the coefficient of variation (COV) was 0.04. The shear capacity of the test results agrees well with the numerical simulation. The FEM has been proved as a reliable numerical method to simulate the shear response of specimens. Therefore, the FEM can be applied to the parametric design-oriented study and also can be researched for the effects of main parameters on the shear behavior.

4. Parameter Analysis

Table 4 shows the finite element simulation results. In this study, a total of 21 finite element models of SRC deep beams are established. According to the validated finite element models, a parametric analysis was executed to study the influence of stirrup spacing, concrete tensile strength f_t, shear span-to-depth ratio λ, the longitudinal reinforcement ratio ρ, flange width of the steel skeleton, and steel skeleton height on the shear capacity. The effects of different parameters on the shear strength of the specimens are discussed hereinafter.

4.1. Influence of Concrete Tensile Strength f_t. Five finite element models were established to research the influence of f_t on the shear capacity of specimens. According to the code GB 50010-2010 [20], the tensile strength of five beams is 2.01, 2.39, 2.64, 2.85, and 2.99 MPa corresponding to C30, C40, C50, C60, and C70 grade concrete, respectively. It can be clear from Table 4 that f_t has a large influence on the shear capacity. When f_t increased from 2.01 to 2.39 MPa, the shear capacity increased by 10%. As the concrete tensile strength varied from 2.85 to 2.99 MPa, the shear capacity increased by 2.7%. The shear capacities of specimens increase with f_t. But, as f_t further increases, the shear capacity of the specimen changes slowly.

4.2. Influence of Shear Span-to-Depth Ratio λ. The influence of λ on the shear capacity was studied on four FEM specimens with various λ of 1.1, 1.4, 1.7, and 2, respectively, as shown in Table 4. When λ increases from 1.1 to 2, the shear capacity decreases from 421 kN to 292 kN. This shows that λ is mainly a factor affecting the shear capacity. On the other hand, the failure mode of the specimen also varies with λ. When λ is less than 1.4, the specimen suffers from diagonal compression failure. And when λ is between 1.4 and 2, the shear failure occurred.

4.3. Influence of Flange Width of Steel Skeleton. Table 4 provides the results of the shear capacity of the simulated SRC deep beams with five ratios of steel skeleton flange width to the beams section width equal to 0.33, 0.42, 0.5, 0.58, and 0.67. It clearly shows that the increase of the width ratio slightly enhanced the shear capacity. The shear
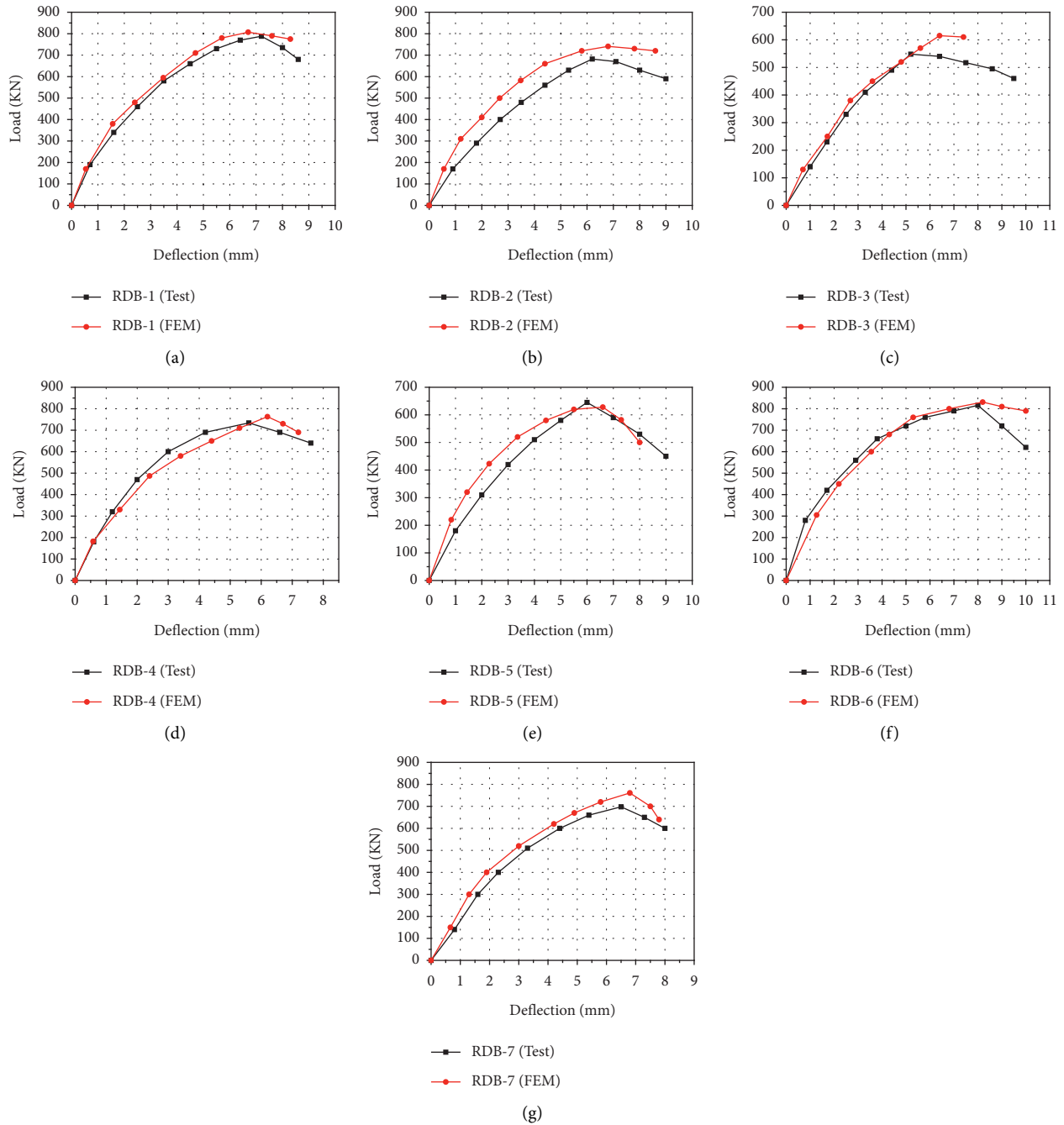
FIGURE 9: The load-deflection curves are compared between experimental and the FEM. (a) RDB-1. (b) RDB-2. (c) RDB-3. (d) RDB-4. (e) RDB-5. (f) RDB-6. (g) RDB-7.

capacity increased by 5.7% when the width ratio varied from 0.33 to 0.5. But with the increase of the width ratio from 0.5 to 0.67, the shear capacity increased by 2.8% only. With the further increase of flange width of the steel skeleton, there is no noticeable increase in the shear capacity. This may be because the steel skeleton flange is arranged at the bottom of the beams, which is mainly subjected to tensile stress and has little contribution to the shear resistance of the specimens.

4.4. Influence of Steel Skeleton Height. Four FEMs were implemented to research the steel skeleton height on the shear capacity of SRC beams. Table 4 shows that the steel skeleton height had a noticeable effect on the shear capacity. There are a total of four different ratios of steel skeleton height to beam section height of 0.3, 0.45, 0.6, and 0.75, respectively. When the height ratio increases from 0.3 to 0.75, the shear capacity of the specimens increases from 284 kN to 474 kN. With an average 36% increase in steel

skeleton height, the shear capacity increased by 18.8% on average. Thus, the steel skeleton web provides a great contribution to shear capacity and shows an important shear behavior in SRC deep beams.

4.5. Influence of Longitudinal Reinforcement Ratio ρ. The change of the shear capacity under different longitudinal reinforcement ratios ρ is shown in Table 4. It clearly shows that ρ between 1% and 2% has no obvious influence. But, when ρ increased from 0.5% to 1%, the shear capacity increased by 14.1%. Low-reinforced SRC deep beams are prone to bending damage. With the increase of ρ, from low-reinforced to overreinforced, the specimens change from flexural failure to shear failure. However, when ρ increased by more than 1%, further increasing ρ has no obvious influence on the specimens. At this point, the longitudinal reinforcement and the steel skeleton flange seem to have the same influence on the shear performance.

4.6. Influence of Stirrup Spacing. The influence of stirrup spacing on the shear capacity of SRC beams was investigated by four finite element models. Table 4 presents the results of the finite element predicted. There are a total of four different values of stirrup spacing of 50 mm, 75 mm, 100 mm, and 125 mm, respectively. It clearly shows that shear capacity decreases with the increase of stirrup spacing. Increasing stirrup spacing from 50 mm to 75 mm decreased the shear capacity by 1%. As the stirrup spacing changed from 75 to 100 mm, the shear capacity of the specimens reduced by 0.5%. And when the stirrup spacing varied from 100 to 125 mm, the shear capacity decreased by 1.3%. Thus, compared with other parameters, the stirrup spacing has a minimal influence.

5. Proposed Method and Verification

5.1. Proposed Method. For SRC structures, the strength superposition theory usually assumes that the shear strength is the sum of the steel skeleton web and the reinforced concrete portion. Furthermore, the strength superposition theory is widely applied to many codes to calculate the SRC slender beams only, not deep beams. There are many factors to consider when using this theory to make theoretical predictions. According to the experiment and finite element analysis in this paper, concrete tensile strength, flange width of the steel skeleton, shear span-to-depth ratio, and steel skeleton height have a relatively large influence on the shear capacity. The stirrup pacing has a slight influence on shear capacity. To ensure the comprehensiveness and accuracy of the calculation results, all of the above influencing parameters have been considered. In this paper, the shear capacity V_{cal} can be assumed to consist of four parts: V_c is the shear capacity contributed by concrete, V_s is the shear capacity contributed by the stirrup, V_{sw} is the shear capacity contributed by steel skeleton web, and V_f is the shear capacity contributed by steel skeleton flange.

It can be observed that V_c decreases with the increase of λ and increases with the increase of f_t. The shear capacity contributed by the concrete portion V_c can be estimated as follows:

$$V_c = \frac{\beta f_t}{\alpha \lambda} bh, \tag{6}$$

where h is the specimen height, b is the specimen width, and β and α are the impact coefficients of f_t and λ, respectively.

According to the experiment and FEM analysis results, the relation of impact coefficient β and α can be estimated as

$$\frac{\beta}{\alpha} = 1.92. \tag{7}$$

It is clearly shown from Table 4 that the shear capacity decreases with the increase of stirrup spacing, but not much impact. Thus, the shear capacity contributed by stirrup V_s can be defined as

$$V_s = 0.11 f_{yv} \frac{A_{sw}}{s} h, \tag{8}$$

where f_{yv} is the yield strength of stirrups, A_{sv} is the area of the stirrups, and s is the stirrup spacing.

The data obtained in the previous section showed that the steel skeleton web had a noticeable effect on the shear capacity. By studying the law of change and linear fitting, the shear capacity contributed by steel skeleton web V_{sw} can be estimated as follows:

$$V_{sw} = 0.43 t_w f_w h_w, \tag{9}$$

where t_w is the web thickness of steel skeleton, f_w is the yield strength of steel skeleton web, and h_w is the height of steel skeleton web.

Many scholars have only studied the shear behavior of the steel skeleton web, but not the shear behavior of the steel skeleton flange. According to the results of this study, as a part of the steel skeleton, the steel flange shows relatively good shear resistance. Therefore, shear capacity contributed by steel skeleton flange V_f cannot be ignored, and it can be estimated exactly as

$$V_f = 0.14 b_f t_f f_{fv}, \tag{10}$$

where b_f is the width of the steel skeleton flange, t_f is the thickness of the steel skeleton flange, and f_{fv} is the yield strength of the steel skeleton flange.

Thus, the shear capacity of SRC deep beams V_{cal} is expressed as follows:

$$V_{cal} = 1.92 \frac{f_t}{\lambda} bh + 0.11 f_{yv} \frac{A_{sv}}{s} h + 0.43 t_w f_w h_w + 0.14 b_f t_f f_{fv}. \tag{11}$$

5.2. Verification of the Proposed Method. The test results of 24 specimens are used to verify the accuracy of the prediction method. These test results are from Chen et al. [11], Deng et al. [24], Wang [25], and Liang [26], respectively. All the specimens are simply supported. Their failure modes are a shear failure and diagonal

TABLE 4: The shear capacity obtained by FEM.

Specimens	Specimen length (mm)	λ	Width ratio	Height ratio	f_t (MPa)	ρ (%)	Stirrup spacing (mm)	Shear capacity (mm)
SDB-1	860	1.1	0.5	0.6	2.39	1.5	100	421 kN
SDB-2	1020	1.4	0.5	0.6	2.39	1.5	100	387 kN
SDB-3	1200	1.7	0.5	0.6	2.39	1.5	100	346 kN
SDB-4	1350	2	0.5	0.6	2.39	1.5	100	292 kN
SDB-5	1020	1.4	0.33	0.6	2.39	1.5	100	365 kN
SDB-6	1020	1.4	0.42	0.6	2.39	1.5	100	374 kN
SDB-7	1020	1.4	0.58	0.6	2.39	1.5	100	393 kN
SDB-8	1020	1.4	0.67	0.6	2.39	1.5	100	398 kN
SDB-9	1020	1.4	0.5	0.3	2.39	1.5	100	284 kN
SDB-10	1020	1.4	0.5	0.45	2.39	1.5	100	353 kN
SDB-11	1020	1.4	0.5	0.75	2.39	1.5	100	474 kN
SDB-12	1020	1.4	0.5	0.6	2.01	1.5	100	352 kN
SDB-13	1020	1.4	0.5	0.6	2.64	1.5	100	414 kN
SDB-14	1020	1.4	0.5	0.6	2.85	1.5	100	438 kN
SDB-15	1020	1.4	0.5	0.6	2.99	1.5	100	456 kN
SDB-16	1020	1.4	0.5	0.6	2.39	0.5	100	333 kN
SDB-17	1020	1.4	0.5	0.6	2.39	1	100	380 kN
SDB-18	1020	1.4	0.5	0.6	2.39	2	100	390 kN
SDB-19	1020	1.4	0.5	0.6	2.39	1.5	50	393 kN
SDB-20	1020	1.4	0.5	0.6	2.39	1.5	75	389 kN
SDB-21	1020	1.4	0.5	0.6	2.39	1.5	125	382 kN

TABLE 5: Experimental verification.

Data sources	Beam	λ	V_{test} (kN)	V_{cal} (kN)	V_{test}/V_{cal}
This paper	RDB-1	1.1	394	366	1.08
	RDB-2	1.4	341	322	1.06
	RDB-3	1.7	274	294	0.93
	RDB-4	1.1	367	332	1.11
	RDB-5	1.1	313	298	1.05
	RDB-6	1.1	408	376	1.09
	RDB-7	1.1	349	355	0.98
Chen et al. [11]	B-H1	1.04	2423	1998	1.21
	B-H2	1.08	2399	1958	1.23
	BW-H2A	1.11	2281	2134	1.07
	BW-H2B	1.09	2605	2369	1.1
	B-H3	1.11	2109	1890	1.12
	B-H4	1.15	1766	1760	1
Deng et al. [24]	C-1	1	650	578	1.12
	C-1.5	1.5	473	426	1.11
	C-2	2	355	350	1.01
Wang [25]	SBI-1	1	400	358	1.12
	SBI-2	1.5	260	292	0.89
	SBI-3	2	240	259	0.92
Liang [26]	SRC-18	1	475	469	1.01
	SRC-19	1.5	310	356	0.87
	SRC-21	1.5	350	370	0.95
	SRC-22	1.5	345	391	0.88
	SRC-23	1.5	350	336	1.04
				AVG	1.04
				COV	0.09

compression failure. The section height of the test piece is 200 mm–550 mm, and there are no shear studs. λ varied from 1 to 2.

Table 5 and Figure 10 compare the tested shear capacity V_{test} with the calculated shear capacity V_{cal} of the suggested method. It can be shown that the calculated results are basically consistent with the experimental. The mean and coefficient of variation are 1.08 and 0.07, respectively. The suggested method can reasonably calculate the shear capacity of SRC deep beams.
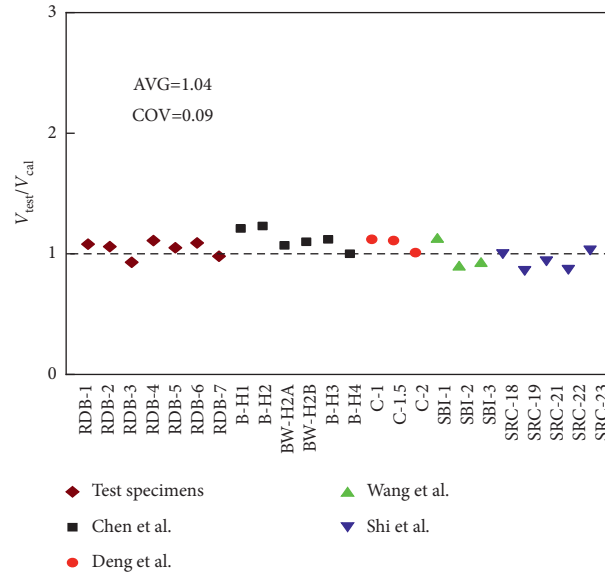
FIGURE 10: Comparison of test values with calculated values.

6. Conclusions

The shear behavior and failure modes of SRC deep beams have been studied by experiment and finite element analysis. The DIC technique was used to record the shear cracking response, initial crack load and location, crack pattern, and track the crack development. Furthermore, the FEM was used to research the influence parameters including the concrete tensile strength f_t, shear span-to-depth ratio λ, stirrup spacing, the longitudinal reinforcement ratio ρ, flange width of the steel skeleton, and steel skeleton height on the shear capacity. In addition, based on the strength superposition theory, the calculation method was recommended for calculating the shear capacity of SRC deep beams.

When the effects of each investigated parameter on failure modes and the shear capacity of SRC deep beams are evaluated in terms of test results and finite element analysis perspective, the following conclusions are deduced:

(1) The failure modes of SRC deep beam under concentrated load can be concluded as two forms: hear failure and diagonal compression failure. When λ is less than 1.4, the specimen suffers from diagonal compression failure. When λ is between 1.4 and 2, shear failure occurred

(2) The DIC technology is proved to be a reliable tool for recording the load at the first crack and track the cracks continuously. Using DIC technology can better understand the shear cracking response and the crack pattern of specimens

(3) The finite element model analysis can accurately simulate the shear response of SRC deep beams. The shear capacity simulated by the finite element models is consistent with the test results. Excellent similarity in load-displacement curves and the failure mode is recorded between finite element analysis and experiment

(4) The shear capacity of SRC deep beams is mainly affected by λ and the height of the steel skeleton web. The shear capacity increases with the increase of the height of the steel skeleton web and decreases with the increase of λ. With an average 36% increase in web height, the shear capacity increased by 18.8% on average. Therefore, under the premise of satisfying the specification, increasing the height of the section web can improve the shear capacity of the SRC deep beams

(5) The proposed calculation method can predict accurate shear strengths of SRC deep beams. A compiled database, which consisted of the 24 SRC deep beams, is used to validate the proposed calculation method. The mean ratio of predicted to tested shear strength and its coefficient of variation is 1.04 and 0.09, respectively.

Data Availability

The data used to support the findings of this study are available from the corresponding author upon request.

Conflicts of Interest

The authors declare that there are no conflicts of interest with respect to the research, authorship, and/or publication of this article.

Acknowledgments

References

[1] H. Chen, W.-J. Yi, and H.-J. Hwang, "Cracking strut-and-tie model for shear strength evaluation of reinforced concrete deep beams," *Engineering Structures*, vol. 163, pp. 396–408, 2018.

[2] A. N. Hanoon, M. S. Jaafar, S. R. Al Zaidee, F. Hejazi, and F. N. A. A. Aziz, "Effectiveness factor of the strut-and-tie model for reinforced concrete deep beams strengthened with CFRP sheet," *Journal of Building Engineering*, vol. 12, pp. 8–16, 2017.

[3] L. Zhou and S. Yi-sheng, "Experimental study on seismic behavior of SRC deep beam-to-CFST column frames," *Journal of Constructional Steel Research*, vol. 155, pp. 157–175, 2019.

[4] L. Zeng, Y. Xiao, J. Chen, and Y. Chen, "Quasi-static cyclic test on a concrete-encased frame-reinforced concrete tube building model," *Shock and Vibration*, vol. 2018, Article ID 5643872, 14 pages, 2018.

[5] Y. Xu, H. Zheng, and J. Ma, "Experimental and analytical research on the hysteretic behavior of steel plate deep beams infill steel frame," *Journal of Constructional Steel Research*, vol. 127, pp. 66–76, 2016.

[6] J. Mo and L. Zeng, "Experimental study on damping properties of rubber powder modified styrene-acrylic emulsion concrete beam," *Journal of Structural Engineering*, vol. 32, Article ID 101728, 2020.

[7] L. Tong, S. Xiao, L. He, Y. Zhang, and X.-L. Zhao, "Fatigue behavior of steel reinforced concrete (SRC) beams with different shear span-to-depth ratios," *Engineering Structures*, vol. 166, pp. 339–353, 2018.

[8] L. Zeng, W. Ren, Z. Zou, Y Chen, W Xie, and X Li, "Experimental study on seismic behavior of frame structures composed of concrete encased columns with L-shaped steel section and steel beams," *Earthquakes and structures*, vol. 16, no. 1, pp. 97–107, 2019.

[9] ACI (American Concrete Institute), "ACI 318-19 & ACI 318R-19: building code requirements for structural concrete and commentary," American Concrete Institute, Farmington Hills, Michigan, USA, 2019.

[10] W.-Y. Lu, "Shear strength prediction for steel reinforced concrete deep beams," *Journal of Constructional Steel Research*, vol. 62, no. 10, pp. 933–942, 2006.

[11] C.-C. Chen, K.-T. Lin, and Y.-J. Chen, "Behavior and shear strength of steel Shape reinforced concrete deep beams," *Engineering Structures*, vol. 175, pp. 425–435, 2018.

[12] British Standards Institution, *Eurocode 2: Design of Concrete Structures: Part 1–1:General Rules and Rules for Buildings*, British Standards Institution, London, UK, 2004.

[13] S. J. Hwang and H. J. Lee, "Strength prediction for discontinuity regions failing in diagonal compressions by softened strut-and-tie model," *Journal of Structural Engineering*, vol. 128, no. 1519, p. 12, 2002.

[14] Architectural Institute of Japan, *AIJ Standard for Structural Calculation of Steel Reinforced Concrete Structures*, Architectural Institute of Japan, Tokyo, Japan, 2001.

[15] JGJ 138-2016, *Code for Design of Composite Structures*, China Architecture and Building press, Beijing, China, 2016.

[16] C. C. Weng and H. S. Wang, "Shear strength of steel reinforced concrete (SRC) deep beams," *Journal of the Chinese Institute of Civil and Hydraulic Engineering*, vol. 16, no. 3, pp. 403–414, 2004, in Chinese.

[17] B. V. Mai, C. H. Pham, G. J. Hancock, and G. D. Nguyen, "Block shear strength and behaviour of cold-reduced G450 steel bolted connections using DIC," *Journal of Constructional Steel Research*, vol. 157, pp. 151–160, 2019.

[18] Z. Huang, Y. Tu, S. Meng, C. Sabau, C. Popescu, and G. Sas, "Experimental study on shear deformation of reinforced concrete beams using digital image correlation," *Engineering Structures*, vol. 181, pp. 670–698, 2019.

[19] Gb/T 50081, *Standard for Test Methods of concrete Physical and Mechanical Properties*, China Architecture and Building Press, Beijing, China, 2019.

[20] GB 50010-2010, *Code for Design of concrete Structures*, China Architecture and Building press, Beijing, China, 2015.

[21] J. Lubliner, J. Oliver, S. Oller, and E. Oñate, "A plastic-damage model for concrete," *International Journal of Solids and Structures*, vol. 25, no. 3, pp. 299–326, 1989.

[22] J. Lee and G. L. Fenves, "Plastic-damage model for cyclic loading of concrete structures," *Journal of Engineering Mechanics*, vol. 124, no. 8, pp. 892–900, 1998.

[23] Z. Tao, Z.-B. Wang, and Q. Yu, "Finite element modelling of concrete-filled steel stub columns under axial compression," *Journal of Constructional Steel Research*, vol. 89, pp. 121–131, 2013.

[24] M. Deng, F. Ma, B. Li, and X. Liang, "Analysis on shear capacity of SRC deep beams based on modified strut-and-tie model," *Engineering Mechanics*, vol. 34, no. 12, pp. 95–103, 2017, in Chinese.

[25] Z. Wang, *Study on Cracks and Deflections of Steel Reinforced concrete Beams*, Xi'an University of Architecture and Technology, Xi'an, China, 2006, in Chinese.

[26] S. Liang, *Experimental Study and Theory Analysis on Stiffness and Crack of Steel Reinforced High Strength-High Performance concrete Beams*, Xi'an University of Architecture and Technology, Xi'an, China, 2007, in Chinese.